Nano Research

Open Access

Research Article

Manipulating spin polarization by *in-situ* reconstructed amorphous/crystalline CoFe-LDH for efficient electrocatalytic water splitting

Cheng Gong[1], Weixin Li[1] ✉, Xing Du[1], Xuan He[1], Daheng Wang[1], Hui Chen[1], Wei Fang[1], Lei Zhao[1] ✉, and Yang Chai[2] ✉

[1] *Faculty of Materials, State Key Laboratory of Advanced Refractories, Wuhan University of Science and Technology, Wuhan 430081, China*
[2] *Department of Applied Physics, The Hong Kong Polytechnic University, Hong Kong 999077, China*

Cite this article: *Nano Research*, **2025**, *18*, 94907668. https://doi.org/10.26599/NR.2025.94907668

ABSTRACT: The performance of oxygen electrocatalysis is dependent on spin-related electron transfer behavior and orbital interactions. Herein, we report a simple spin-polarized approach to enhance the oxygen evolution reaction (OER) process of CoFe-layered double hydroxide (LDH). The amorphous/crystalline CoFe-LDH nanosheets (a/c-CoFe-LDH) are prepared via acid-etching assisted co-precipitation to construct abundant amorphous/crystalline interfaces. The a/c-CoFe-LDH with controlled amorphous degree leads to manipulable magnetism, thus altering symmetric distribution of the d-orbital spin-electron states and facilitating spin-selective electron transfer process. The adsorbed O species will predominantly settle on a fixed spin direction, which propels the production of triplet oxygen. As a result, the amorphous/crystalline heterostructure contributes to suitable d-band centers, thus optimizing the adsorption strengths of oxygen-generated intermediates. Besides, the unsaturated coordination metals induce the generation of oxygen non-bonding states, thus prompting oxygen as the redox center and triggering the lattice oxidation mechanism (LOM). Meanwhile, the crystalline structure endows excellent intrinsic conductivity and persistent stability. The obtained a/c-CoFe-LDH achieves low overpotentials of 269 mV at 10 mA·cm^{-2} in 1.0 M KOH towards the OER. To further enhance hydrogen evolution reaction (HER) performance, Pt nanocluster was introduced into a/c-CoFe-LDH. This study offers a controllable method to prepare amorphous/crystalline electrocatalysts with regulated spin configuration for efficient water splitting.

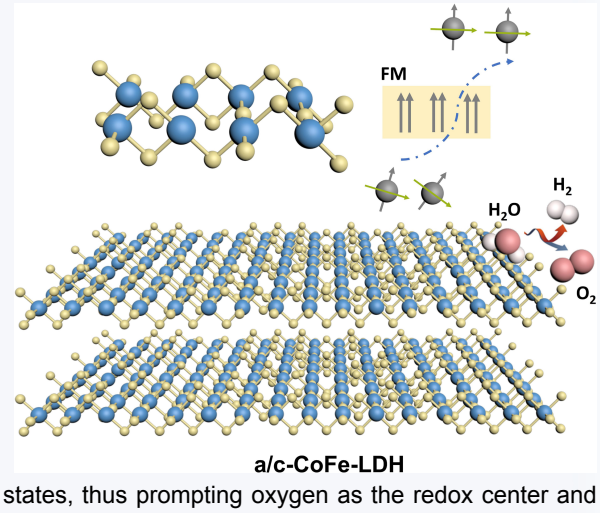

KEYWORDS: amorphous/crystalline, acid etching, spin configuration

1 Introduction

To satisfy the requirements of low-carbon living, hydrogen energy obtained via electrochemical water splitting is paramount [1]. However, the anodic oxygen evolution reaction (OER) involved a complex four-electron transfer process and additional energy barrier from spin flip, resulting in sluggish kinetics which limits the water splitting process [2, 3]. Hence, the design of oxygen electrocatalysis requires consideration of both orbital interactions and electron transfer behavior. Layered double hydroxides (LDHs) are regarded as potential alternatives to noble catalysts owing to their adaptable composition, flexible open structure, and tunable electronic structure [4, 5]. Due to the saturated metal–oxygen (M–O) bonds in MO_6 structure of LDH, reaction between OH^-/H_2O and the active site is hindered, leading to undesirable charge transfer. Hence, the limited number of exposed active sites and poor intrinsic electrocatalytic activity are the main challenges for LDH [6].

Compared to the singlet state of OH^-/H_2O with all paired electrons, the generated O_2 is a triplet state (↑O=O↑), where the frontier π^* orbitals are occupied by two electrons with parallel

Received: March 25, 2025; **Revised:** June 1, 2025
Accepted: June 5, 2025

✉Address correspondence to Weixin Li, liweixin@wust.edu.cn; Lei Zhao, zhaolei@wust.edu.cn; Yang Chai, y.chai@polyu.edu.hk

alignment, which has the lowest energy. The reaction from OH^-/H_2O to O_2 requires spin-related electron transfer, which has a significant effect on the reaction kinetics. The spin-polarized electrons in electrocatalysts facilitate the generation of parallel spin-aligned oxygen by quantum spin-exchange interactions (QSEI), thus boosting the catalytic activity of OER [7]. The adsorption behavior of the intermediates is strongly relevant to the spin state of the active sites, which directly influences electron transfer process and reaction energy barrier [8]. Therefore, the adjustment of spin configuration is an attractive strategy for the design of LDH electrocatalysts with enhanced OER performance.

Different degree of crystallinity induces diversities in the coordination structure of the active sites and alters the periodicity of the crystal structure [9]. The amorphous phases possess abundant unsaturated coordination configurations and dangling bonds, which can modify the spin state of the catalyst [10, 11]. For example, previous report discovered that spin state of Co^{2+} transforms from high spin (HS) to low spin (LS) with the decrease of crystallinity of $CoNiO_2$ [12]. The asymmetric distribution of the d-orbital spin-electron states near the Fermi energy level could regulate the spin states to enhance catalytic activity [13]. The enhanced interatomic ferromagnetic (FM) coupling implies a direct correlation between spin-selective charge transfer mobility and catalytic activity, thus enhancing OER. Besides, the unsaturated coordination metals induce the generation of oxygen non-bonding states, which is in favor for prompting oxygen as the redox center [14, 15]. Consequently, the regulation of electron spin and orbital interactions induces both metal and lattice oxygen to participate in catalytic reactions simultaneously, thus reducing the reaction energy barrier [16, 17]. Although amorphous structure provides a platform for the regulation of spin configuration and modulation of OER mechanism, the relatively inferior intrinsic conductivity and poor stability of amorphous materials remain the bottleneck for efficient electrocatalysis [9]. The construction of catalysts with crystalline/amorphous heterostructures can inherit the plentiful unsaturated coordination active sites of amorphous materials, as well as the desirable intrinsic conductivity and persistent stability of crystalline material. In addition, the amorphous–crystalline heterointerfaces combine the merits of increased active sites with shorten diffusion path of ions and electrons, thus further improving catalytic activity and stability [18]. However, controllable amorphous structure with modulated electron spin state remains a challenge.

Herein, we report a spin-polarized strategy to prepare an amorphous/crystalline CoFe-LDH nanosheets (a/c-CoFe-LDH) by an acid-etching and coprecipitation method. The a/c-CoFe-LDH with controlled amorphous degree by *in-situ* reconstruction can induce more spin-polarized electrons. The adsorbed O species predominantly settle on a fixed spin direction, thus promoting the production of triplet oxygen. The participation of oxyl radicals with additional unpaired non-bonding p electrons is considered crucial for spin polarization in OER, thus reducing the barrier for subsequent –O–O– coupling (rate-determining step (RDS)). The unsaturated coordination of amorphous CoFe-LDH accompanied by oxygen non-bonding state triggers the lattice oxidation mechanism (LOM). Hence, metal and lattice oxygen redox pairs simultaneously serve as active sites to accelerate OER kinetics. Meanwhile, the crystalline structure endows excellent intrinsic conductivity and persistent stability. To enhance the hydrogen evolution reaction (HER) catalytic activity, Pt nanocluster was loaded in a/c-CoFe-LDH. This study provides a novel strategy to rationally tailor the orbital interaction between the spin-dependent catalyst and the intermediate, which can alter the RDS and reaction pathway for efficient electrocatalytic water splitting.

2 Experimental

2.1 Synthesis

2.1.1 CoFe-LDH preparation

$Co(NO_3)_2{\cdot}6H_2O$ (0.88, 1.16, 1.46, 1.75, and 2.00 g, respectively), $FeCl_2{\cdot}4H_2O$ (0.99, 0.79, 0.59, 0.39, and 0.19 g, respectively), and urea (1.30 g) were dispersed in 50 mL of methanol and 10 mL of deionized water mixed solution. After stirring for 30 min, the mixture was transferred into a stainless-steel autoclave and heated at 150 °C for 8 h. The obtained CoFe-LDH-*n* (*n* = 3:5, 4:4, 5:3, 6:2, and 7:1) was washed thoroughly and dried for further use. Among them, CoFe-LDH-5:3 was defined as CoFe-LDH.

2.1.2 a/c-CoFe-LDH preparation

40.0 mg of CoFe-LDH power was dispersed in 40 mL (including 0.0, 0.6, 0.8, and 1.0 mL acetic acid, respectively) of acetic acid solution. After stirring for 40 min, 30.0 mg $NaBH_4$ was added and kept stirring for 30 min. The brown product washed thoroughly was named as a/c-CoFe-LDH-*x* (*x* = 0.0, 0.6, 0.8, and 1.0). Among them, a/c-CoFe-LDH-0.8 was defined as a/c-CoFe-LDH.

2.1.3 a/c-CoFe-LDH/Pt preparation

a/c-CoFe-LDH/Pt was synthesized by the same procedure as that of a/c-CoFe-LDH but adding additional 10.0 mg H_2PtCl_6 in acetic acid solution.

2.2 Characterization

The morphology information was observed by field emission scanning electron microscopy (FESEM, Nova400 Nano SEM), transmission electron microscopy (TEM, JEM-2100F, Japan), and atomic force microscopy (AFM, Dimension icon, Bruker AXS). The crystal structure was analyzed using X-ray diffractometer (XRD, X'Pert Pro, Philips, Netherlands). The surface valence and electronic interaction of the catalysts were assessed using X-ray photoelectron spectroscopy (XPS, Thermo Fisher Scientific, England). The magnetic properties of the samples were evaluated by vibrational sample magnetometer (VSM, LakeShore7404, USA) in the range of −5000 to 5000 Oe at room temperature. The functional groups of the obtained samples were investigated by Fourier transform infrared (FTIR, ThermoScientific Nicolet iS50). The Raman spectra were collected by a Raman spectrometer (DXR2xi, ThermoFisher). Brumauer–Emmett–Teller (BET, JW-BK132F) analysis was performed to analyze the surface area and pore structures. The mass content of the as-prepared electrocatalysts was quantified by inductively coupled plasma-mass spectrometry (ICP-MS, PerkinElmer NexION 300X). The produced H_2 and O_2 were collected by gas chromatography (CEAULIGHT, GC-7920).

2.3 Electrochemical measurements

All electrochemical measurements were conducted on a CHI 660E potentiostat in a three-electrode configuration without *IR* compensation correction. Among the three electrodes, glassy

carbon electrode (radius of 2 mm) served as the working electrode, Hg/HgO (in KOH solution) was used as the reference electrode, and platinum plate was used as the counter electrode. The electrocatalyst inks were prepared by dispersing 4.0 mg of catalysts and 1.0 mg of carbon black in 700 μL of ethanol and 50 μL of Nafion, followed by ultrasonication for 60 min. Subsequently, 15 μL of ink was deposited onto the surface of glassy carbon electrode. The linear sweep voltammetry (LSV) was recorded at a scan rate of 5 $mV \cdot s^{-1}$ in 1.0 M KOH solution. The potentials were converted to the reversible hydrogen electrode (RHE) using $E_{(vs.\ RHE)} = E_{(vs.\ Hg/HgO)} + 0.059pH + 0.098$. The electrochemically active surface area (ECSA) was carried out with double-layer capacitance (C_{dl}) deduced from scan-rate dependence of cyclic voltammograms (CVs). Electrochemical impedance spectroscopy (EIS) was performed with the frequency from 0.01 Hz to 100 kHz. Turnover frequency (TOF) was obtained according to the equation: TOF = $jS/4Fn$ (OER) or TOF = $jS/2Fn$ (HER), where j ($A \cdot cm^{-2}$) is the current density at η = 300 mV, S (cm^{-2}) is the surface area of glassy carbon electrode, F is the Faraday constant (96485 $C \cdot mol^{-1}$), and n is the number of electron transferred for the evolution of a single O_2/H_2 molecule. Laviron equation is $E_p = E_{1/2} - (RT/\alpha nF) \times \ln(\alpha nF/RTk_s) - (RT/\alpha nF) \times \ln(\nu)$, where E_p is the reduction potential of metal redox, $E_{1/2}$ is the formal potential of metal redox, R is the universal gas constant, T is the temperature in Kelvin, α is the transfer coefficient, k_s is the rate constant of metal redox, and ν is the scan rate in the CV measurements [19].

2.4 Theoretical calculations

The theory computation of density functional theory (DFT) was carried out by using Vienna *ab initio* simulation package (VASP), adopting the projected augmented wave (PAW) method [20]. The Perdew–Burke–Ernzerhof (PBE) functional was used to describe the exchange and correlation effects [21]. For calculation parameters, the cutoff energy was set to be 500 eV and the Monkhorst–Pack scheme was set to be 2 × 2 × 1. In addition, the force tolerance and energy tolerance were 0.01 $eV \cdot Å^{-1}$ and 1.0 × 10^{-5} $eV \cdot atom^{-1}$, respectively. The vacuum space along the z-direction was set to be 15 Å. The Gibbs free energy of the adsorbed intermediates (ΔG_{ads}) was defined as: $\Delta G_{ads} = \Delta E_{ads} + \Delta E_{ZPE} - T\Delta S$, where ΔE_{ads}, ΔE_{ZPE}, and ΔS were the binding energy, zero point energy change, and entropy change of adsorption intermediate, respectively.

3 Results and discussion

The a/c-CoFe-LDH with abundant amorphous/crystalline interfaces was prepared using acid-etching assisted coprecipitation method (Fig. 1(a)). In detail, the pristine CoFe-LDH was etched by acetic acid at room temperature. During this process, part of CoFe-LDH reacts with H^+ to generate metal ions. Next, $NaBH_4$ was induced to further attacks the M–O bond of CoFe-LDHs, leading to the formation of amorphous CoFe-LDHs on the surface of crystalline CoFe-LDHs. The alkaline medium produced by the hydrolysis of $NaBH_4$ ($NaBH_4 + 2H_2O = NaBO_2 + 4H_2\uparrow$) plays a pivotal role in breaking bonds and providing OH^- ions [22]. OH^- produced by hydrolysis of $NaBH_4$ assists the generation of amorphous CoFe-LDH through recrystallization. Electron paramagnetic resonance (EPR) spectra were recorded to illustrate the electronic configuration. In contrast to CoFe-LDH, a pair of distinct peaks can be observed for a/c-CoFe-LDH (Fig. 1(b)). The degree of amorphous state can be reflected by the number of oxygen vacancies. The amorphous degree reaches the maximum value when acid is moderate. The results demonstrate the existence of abundant defective sites associated with unpaired electrons induced by amorphous region [23]. To further illustrate the spin configuration, the field dependence magnetization for CoFe-LDH and a/c-CoFe-LDH-x in the field range of −5000 to 5000 Oe at room temperature was measured. In Fig. 1(c), the FM interaction increases with the increase of amorphous degree. The ferromagnetism of a/c-CoFe-LDH-x leads to the improved catalytic activity. For a FM catalyst, the 3d–2p hybridization inside FM materials will facilitate spin selective charge transport based on QSEI effect [24]. Therefore, the a/c-CoFe-LDH with FM is beneficial for the electron transfer between the adsorbed oxygen species and metal centers [25]. Figures 1(d) and 1(e) and Fig. S1 in the Electronic Supplementary Material (ESM) present the spin-related electron transfer mechanism of a/c-CoFe-LDH. In singlet oxygen species (e.g., OH^- and H_2O), spin-up and spin-down electrons are paired in the p state of oxygen, which retaining transfer capability. Besides, spin-selective electron transfer pathways reduce the energy barrier for triplet oxygen formation by 1.0 eV compared to non-spin-selective routes. The a/c-CoFe-LDH comprises mixed-valent Co^{2+}/Co^{3+} and Fe^{2+}/Fe^{3+} ions coexisting in HS, medium spin (MS), and LS configurations. According to QSEI theory, LS Fe^{3+} ions create spin-selective electron transfer pathways, while HS Co^{2+} ions selectively extract spin-oriented electrons from reactants [26]. This synergistic mechanism drives the formation of a spin-fixed intermediate (O(↓)), which subsequently evolves into the triplet-state O(↓)O(↓)H species, thus enhancing OER performance. What is more, the results of ICP-MS indicate that a/c-CoFe-LDH has a higher Co, Fe/O ratio than that of CoFe-LDH, further suggesting that the original MO_6 structure is broken (Table S1 in the ESM). The defective structure (MO_{6-x}) triggers a spin-state transition in transition metal centers from LS to HS configurations, which is beneficial for enhancing catalytic activity [8, 27–29]. Oxygen vacancies function as electron donors, increasing unpaired electron density in the 3d orbitals of Co and Fe, which leads to the increased content of HS Co and HS Fe states along with enhanced magnetic properties [30, 31]. In addition, oxygen vacancies also bring a large number of spin polarized electrons, accelerating the reaction kinetics. Therefore, CoFe-LDH exhibits a relatively poor electrocatalytic performance than a/c-CoFe-LDH, although CoFe-LDH consists of a higher concentration of LS Fe^{3+}. Compared to CoFe-LDH, a/c-CoFe-LDH exhibits enhanced magnetic moments (Co: 2.98 μB and Fe: 3.71 μB) based on DFT calculations, indicating more unpaired electrons. n can be calculated according to the equation: $\mu=\sqrt{n(n+2)}$, where μ represents the magnetic moments. Therefore, the unpaired electrons of Co and Fe are 2.15 and 2.84, which confirms the presence of HS Co^{2+} and LS Fe^{3+}, demonstrating the existence of spin-related electron transfer mechanism. It is expected that the FM state of a/c-CoFe-LDH endows LS Fe^{3+} ($t_{2g}^5e_g^0$) and HS state Co^{2+} cations ($t_{2g}^5e_g^2$), which can serve as selective gates to remove spin-oriented electrons from the reactants, thus promoting the formation of triplet oxygen [32, 33].

The composition of the as-prepared catalysts was determined by XRD (Fig. S2 in the ESM). For CoFe-LDH, the diffraction peaks at 11.5°, 23.1°, 34.0°, 38.5°, 45.9°, 58.8°, and 60.3° correspond to the CoFe-LDH (PDF No. 00-050-0235). Due to the acid etching and recrystallization, a/c-CoFe-LDH exhibits poor crystallinity, which explains the disappearance of (006) and (015) planes. In contrast,

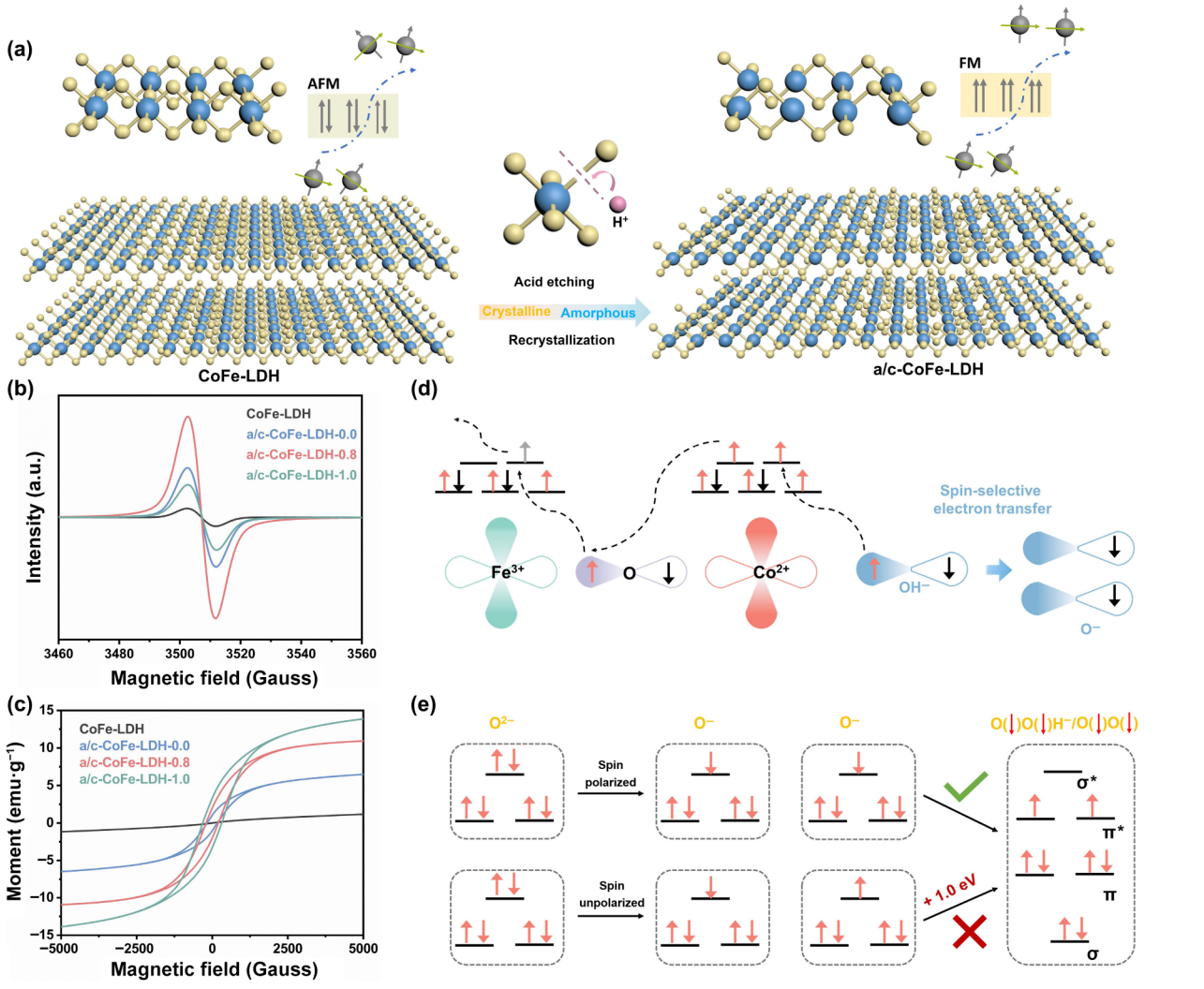

Figure 1 (a) Schematic diagram for the preparation process of a/c-CoFe-LDH. (b) EPR spectra for CoFe-LDH and a/c-CoFe-LDH-x. (c) Hysteresis loops of CoFe-LDH and a/c-CoFe-LDH-*x*. (d) The formation of the triplet intermediate O(↓)O(↓)H/O(↓)O(↓) species. (e) Schematic illustration of the spin-selective channel in a/c-CoFe-LDH.

a/c-CoFe-LDH/Pt shows an extra diffraction peak of 39.8°, corresponding to the (111) plane of Pt (PDF No. 03-065-2868). The results of XRD suggest the formation of a/c-CoFe-LDH/Pt. With the increase of the H^+ concentration, the (006) plane of CoFe-LDH gradually disappears, demonstrating the decreased crystallinity of CoFe-LDH (Fig. S2(b) in the ESM). To qualitatively analyze the amorphous/crystalline ratio, the peak areas of amorphous/crystalline phases in XRD were calculated by integration. As shown in Table S2 in the ESM, the amorphous phase content increases progressively with higher H^+ concentration, which is consistent with the result of EPR. As regard to the nitrogen adsorption–desorption isotherms (Fig. S3 in the ESM), the a/c-CoFe-LDH exhibits increased BET surface area (152.7 $cm^2 \cdot g^{-1}$) and pore volume (0.91 $cm^3 \cdot g^{-1}$). These results can be ascribed to the additional introduced H^+ which reacts with CoFe-LDH and the etches metal ions. With increased acid concentration, the specific surface area of a/c-CoFe-LDH initially increases and then decreases (Fig. S4 in the ESM). This can be ascribed to the fact that excessive acid etches the structure, causing aggregation of particles. The morphologies of CoFe-LDH, a/c-CoFe-LDH, and a/c-CoFe-LDH/Pt are shown in Figs. 2(a)–2(c). The CoFe-LDH exhibits two-dimensional nanosheet structure. After acid etching and recrystallization, a/c-CoFe-LDH still retains the nanosheet structure, except with the reduced size. In addition, the Pt nanoclusters are attached on the surface of a/c-CoFe-LDH/Pt through introduction of H_2PtCl_6. The detailed structure of a/c-CoFe-LDH was further demonstrated by TEM. In Fig. 2(d), the two-dimensional nanosheet feature of the a/c-CoFe-LDH is reconfirmed. As a supplement, the AFM results evaluate that the thickness of the a/c-CoFe-LDH and a/c-CoFe-LDH/Pt nanosheet is approximately 4.9 and 5.1 nm, respectively (Fig. S5 in the ESM). The high-resolution TEM (HRTEM) image of a/c-CoFe-LDH (Fig. 2(e)) reveals visible interfaces, suggesting the formation of amorphous/crystalline heterostructure. The appearance of amorphous regions converted by recrystallization brings abundant defects and inherent disorder MO_{6-x} structural, which promotes interfacial charge transfer and ion diffusion in a/c-CoFe-LDH [34, 35]. The lattice fringes of 2.09 and 2.33 Å correspond to the (117) and (015) planes of CoFe-LDH, respectively. The selected area electron diffraction (SAED) pattern of the a/c-CoFe-LDH displays bright rings. The above results demonstrate amorphous structure integrated with crystalline structure in a/c-CoFe-LDH (Fig. 2(f)). In

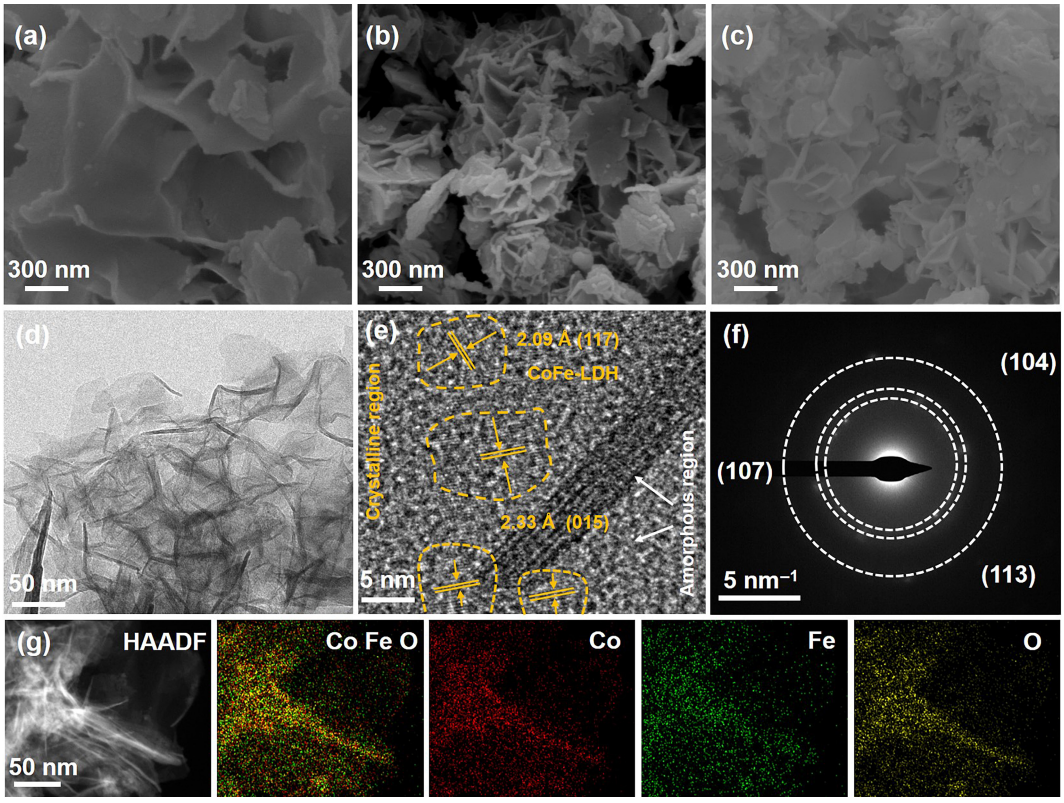

Figure 2 SEM images of (a) CoFe-LDH, (b) a/c-CoFe-LDH, and (c) a/c-CoFe-LDH/Pt. (d) TEM image, (e) HRTEM image, (f) SAED pattern, and (g) elemental mapping images of a/c-CoFe-LDH.

addition, the elemental mapping images indicate the uniformly distributed Co, Fe, and O elements (Fig. 2(g)). Compared with a/c-CoFe-LDH, a/c-CoFe-LDH/Pt maintained the original nanosheet structure with the Pt nanocluster anchored on the surface of nanosheets (Fig. S6(a) in the ESM). As confirmed by HRTEM (Fig. S6(b) in the ESM), the lattice fringes of 1.98, 2.26, and 2.33 Å are ascribed to the (200), (111) planes of Pt and the (015) plane of CoFe-LDH, respectively. Furthermore, the diffraction rings in SAED pattern are assigned to (111) plane of Pt and (113) plane of CoFe-LDH, in consistent with the results of HRTEM image (Fig. S6(c) in the ESM). The interaction between amorphous region and Pt nanocluster can alter the binding energy of intermediates, thus boosting water splitting performance [36].

In Fig. 3(a), all the as-prepared catalysts exist Co, Fe, and O elements. In Fig. 3(b) and Fig. S7(a) in the ESM, the peaks at 780.9 eV ($2p_{3/2}$) and 796.7 eV ($2p_{1/2}$) correspond to Co^{3+}. While the peaks at 782.8 eV ($2p_{3/2}$) and 798.1 eV ($2p_{1/2}$) can be attributed to Co^{2+} [37, 38]. The high-resolution Fe 2p spectra display three typical peaks which can be deconvoluted into Fe^{2+} $2p_{3/2}$, Fe^{3+} $2p_{3/2}$, and Fe^{2+} $2p_{1/2}$, respectively (Fig. 3(c) and Fig. S7(b) in the ESM) [39]. Moreover, the O 1s spectrum of a/c-CoFe-LDH shows three peaks centered at 530.6, 531.7, and 533.1 eV, which can be attributed to M–O, vacancy oxygen (O_v), and absorbed H_2O (Fig. 3(d) and Fig. S7(c) in the ESM) [40]. To be noted, compared with CoFe-LDH (40.5%), the a/c-CoFe-LDH exhibits increased O_v (56.2%) owing to the unsaturated coordination of amorphous CoFe-LDH [17, 41]. Compared with CoFe-LDH, the Co $2p_{3/2}$ and Fe $2p_{3/2}$ peaks in a/c-CoFe-LDH shift towards lower binding energy, which reveals that Co and Fe gain electrons owing to the increased oxygen vacancies. Hence, the MO_{6-x} structure with more oxygen vacancies exhibits stronger catalytic activity owing to the unpaired 3d orbitals. Upon Pt deposition, the Co $2p_{3/2}$ and Fe $2p_{3/2}$ peaks in a/c-CoFe-LDH/Pt shift towards higher binding energy, revealing electron depletion at Co and Fe sites. Electron transfer between a/c-CoFe-LDH and Pt not only regulates the electronic structure of the material but also promotes the interaction between the a/c-CoFe-LDH and Pt, thereby enhancing catalytic activity and stability. As illustrated in Fig. 3(e), the octahedral ligand field results in each metal atom being fully coordinated to six oxygen atoms (MO_6), thus leading to the splitting of the metal d-orbitals into higher-energy e_g and lower-energy t_{2g} states. When the MO_6 structure is disrupted (MO_{6-x}), the unpaired 3d orbitals can interact with and accept lone-pair electrons from the adsorbed intermediates, leading to the enhanced catalytic activity [42]. Based on the Goodenough–Kanamori rule, the electronic hopping between half-filled t_{2g} levels and unfilled e_g levels endows the FM behavior of a/c-CoFe-LDH, which is consistent with result of VSM [43].

In order to evaluate the intrinsic electrocatalytic performance of the as-prepared catalysts, the LSV polarization curves were presented without *IR* compensated correction. In Fig. S8 in the ESM, it can be confirmed that the sample with a Co/Fe ratio of 5:3 shows the best electrochemical performance. The a/c-CoFe-LDH-0.8 displays the best OER catalytic activity among the series of samples, in line with the EPR results (Fig. S9 in the ESM). In Fig. 4(a), a/c-CoFe-LDH displays a low overpotential (η_{10}) of 269 mV, which is superior to that of CoFe-LDH (309 mV) and RuO_2 (395 mV). Besides, a/c-CoFe-LDH/Pt which aims to further enhance the HER activity also exhibits slightly lower overpotential (η_{10}) of 253 mV than that of a/c-CoFe-LDH. The performance of the a/c-CoFe-LDH/Pt is comparable to those LDH based catalysts reported previously (Fig. 4(b)). To evaluate the charge transfer kinetics of the different samples, the Nyquist plots were fitted using

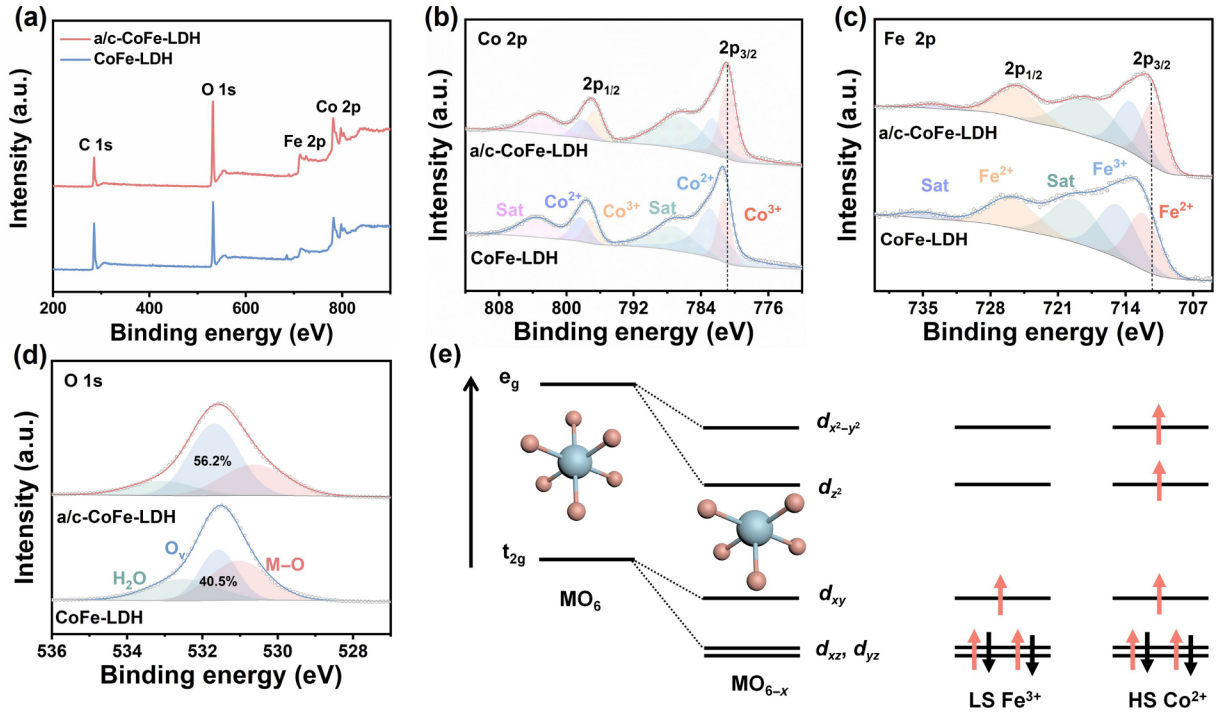

Figure 3 (a) XPS survey spectra. High-resolution XPS spectra of (b) Co 2p, (c) Fe 2p, and (d) O 1s of CoFe-LDH and a/c-CoFe-LDH. (e) Electron configuration of 3d orbital.

an equivalent circuit model. EIS results revealed that a/c-CoFe-LDH (3.77 Ω) exhibits a higher charge transfer resistance (R_{ct}) compared to CoFe-LDH (3.31 Ω), suggesting reduced conductivity due to the amorphous phase (Fig. 4(c)). Besides, the introduction of Pt in a/c-CoFe-LDH/Pt lowered the R_{ct} to 3.21 Ω, attributed to the enhanced interfacial electron transfer kinetics between the electrode and electrolyte. While a/c-CoFe-LDH/Pt exhibits the lowest charge transfer resistance due to the incorporation of Pt nanoclusters. The reaction kinetics of the catalysts are obtained from the Tafel slope in Fig. 4(d). As expected, the Tafel slope of CoFe-LDH, a/c-CoFe-LDH, and a/c-CoFe-LDH/Pt is 85, 74, and 57 mV·dec^{-1}, respectively. The results indicate that the generation of MO_{6-x} structure can promote reaction kinetics. In addition, the ECSA were used to assess catalytic activity. The ECSA were estimated based on the electrochemical C_{dl} obtained from CV. Compared with CoFe-LDH, a/c-CoFe-LDH possessed the larger C_{dl}, indicating that more electrochemically active sites in a/c-CoFe-LDH along with enhanced catalytic activity. Moreover, a/c-CoFe-LDH exhibits higher mass activity (43.0 mA·mg^{-1}) and larger TOF (1.4×10^{-2} s^{-1}) at the overpotential of 300 mV, which revealed the superior catalytic activity of a/c-CoFe-LDH. The value of mass activity and TOF is further improved for a/c-CoFe-LDH/Pt. LSV curves normalized by ECSA are also provided in Fig. S12(a) in the ESM to further illustrate the intrinsic activity of as-prepared catalysts. Among them, a/c-CoFe-LDH/Pt demonstrates the superior catalytic performance, which confirms its highest intrinsic OER activity. Therefore, the construction of amorphous/crystalline interface is favor for improving intrinsic catalytic activity and exposing more active sites, thus accompanied by the promoted kinetics and boosted OER activity. The robust metal–oxygen bonds in crystalline LDHs act as stress buffers to mitigate structural collapse during LOM process. Interfacial charge redistribution between a/c-CoFe-LDH and Pt not only optimizes the electronic configurations but also strengthens interfacial covalent coupling, thereby enhancing overall stability. Therefore, a/c-CoFe-LDH/Pt achieves exceptional operational durability (> 100 h), outperforming pristine a/c-CoFe-LDH and demonstrating viability for industrial water electrolysis systems (Fig. 4(f) and Fig. S17(a) in the ESM). The CV curves show that the redox peak (Co^{2+}/Co^{3+} wave) of a/c-CoFe-LDH undergoes a negative shift owing to the formation of unsaturated coordination metal sites (Fig. S13 in the ESM), revealing the changed electronic structure of a/c-CoFe-LDH [34, 53]. The k_s derived from equation can be used to qualitatively compare the binding strength of OH^- to the as-prepared catalysts in electrolyte. The stable redox currents are linearly related to the square root of the potential sweep rates in CV tests (Fig. 4(e)). The a/c-CoFe-LDH exhibits larger k_s value (0.46 s^{-1}) than that of CoFe-LDH (0.31 s^{-1}), suggesting enhanced adsorption of OH^- owing to the generation of amorphous/crystalline interface [54].

To gain deep insights into OER mechanism, pH-dependence, oxygen intermediate, and *in-situ* Raman spectra were tested. As shown in Fig. S14 in the ESM, a/c-CoFe-LDH presents a strong correlation between the pH value and OER activity at the pH range from 12.5 to 14.0, while CoFe-LDH shows weak pH-dependent activity. To accurately elucidate the relationship between activity and pH values, the proton reaction orders on RHE scale ($\rho_{RHE} = \partial \log(j)/\partial pH$, where ρ_{RHE} represents proton reaction order and pH is potential of hydrogen (pH value)) was adopted [55]. Compared with CoFe-LDH, the ρ^{RHE} value of a/c-CoFe-LDH (0.79) is closer to 1, implying the existence of LOM in OER. The LOM pathway involves O_2^{2-} and O^{2-} negative species, and the O_2^{2-} species can act as an indicator of whether OER proceeds via the LOM pathway. Due to the strong interaction between O_2^{2-} and tetramethylammonium cation (TMA^+), TMA^+ can inhibit the formation of O_2^{2-} [56]. The TMA^+ would bind to O_2^{2-} and impede the LOM pathway, thus restricting OER activity. In Fig. 4(g), the

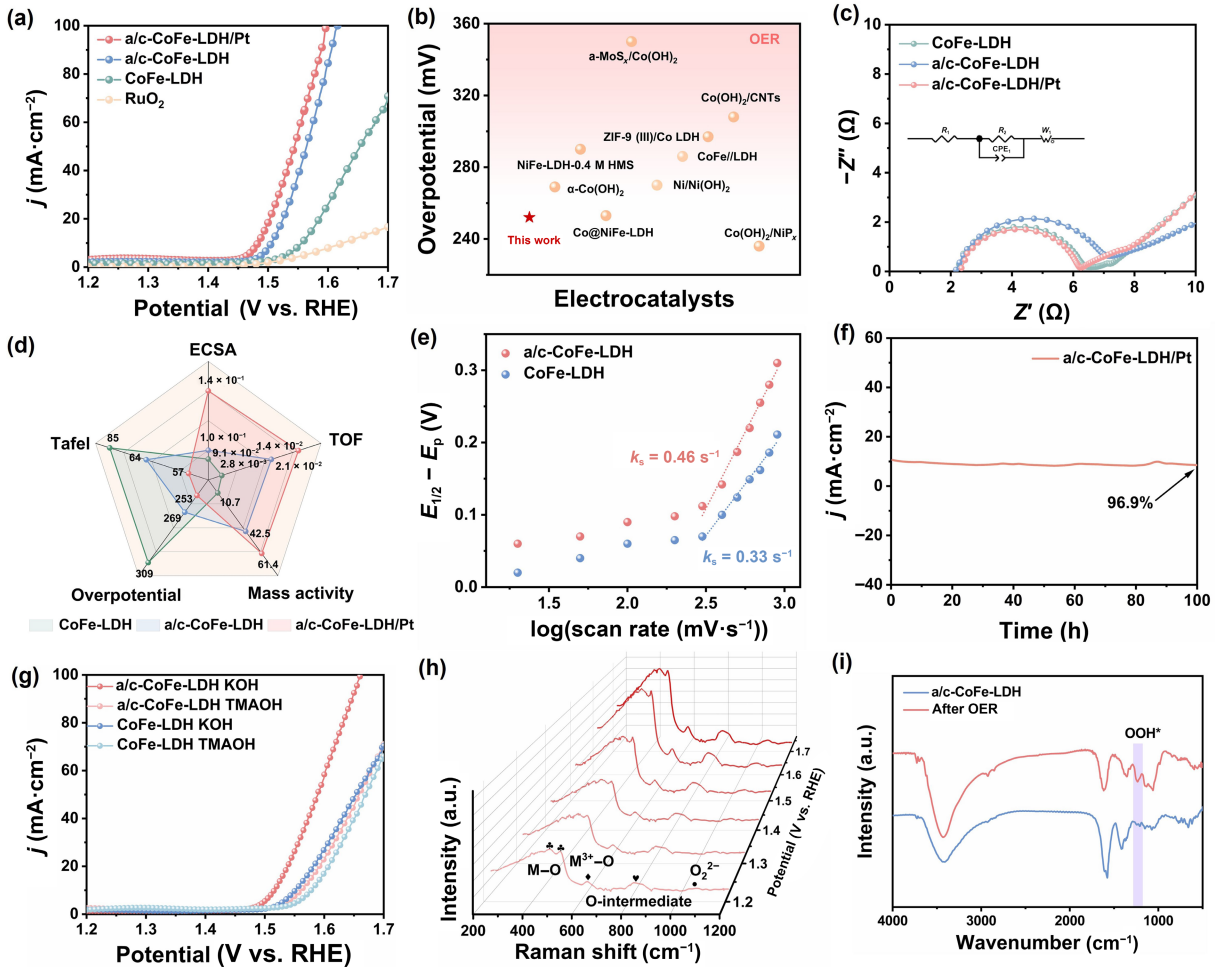

Figure 4 (a) LSV curves of a/c-CoFe-LDH/Pt, a/c-CoFe-LDH, CoFe-LDH, and RuO_2. (b) Comparisons of the OER activity of a/c-CoFe-LDH/Pt with other recently reported LDH based materials [42–52]. (c) Nyquist plots with the fitting curves in OER. (d) Tafel, ECSA, TOF, overpotential and mass activity of a/c-CoFe-LDH/Pt, a/c-CoFe-LDH, and CoFe-LDH. (e) Laviron analysis of CoFe-LDH and a/c-CoFe-LDH. (f) Chronoamperometry test of a/c-CoFe-LDH/Pt in OER for 100 h. (g) LSV curves of CoFe-LDH and a/c-CoFe-LDH in 1.0 M KOH with and without TMAOH. (h) *In-situ* electrochemical-Raman spectra during the OER process of a/c-CoFe-LDH. (i) FTIR spectra of a/c-CoFe-LDH before and after OER.

OER activity of a/c-CoFe-LDH decreases with the addition of TMAOH, implying that presence of LOM pathway in a/c-CoFe-LDH. In addition, *in-situ* Raman spectra of a/c-CoFe-LDH indicate the potential-dependent change of its OER intermediate. The peaks at 441 and 490 cm^{-1} correspond to lattice vibrational modes of M–O bond (Fig. 4(h) and Fig. S15 in the ESM) [57]. In addition, the peaks at 608 and 805 cm^{-1} correspond to M–OH species and the peak at 1061 cm^{-1} corresponds to oxygen-containing intermediates [16, 58]. The Raman peak at 1061 cm^{-1} which is regarded as $*O_2^{2-}$ (*–O–O–*) gradually becomes stronger with the increase of potential, indicating the generation of $*O_2^{2-}$ species and confirming the existence of LOM during OER process [15, 16]. On the contrary, for the original CoFe-LDH, the peak of $*O_2^{2-}$ species shows no significant changes, which implies a dominated adsorbate evolution mechanism (AEM) pathway (Fig. S15 in the ESM) [59]. The nucleophilic reagent methanol is prone to adsorb the electrophilic reagent *OH during the OER process, which is competitive with the adsorption of *OH in OER. Therefore, methanol oxidation reaction (MOR) is regarded as a probe for measuring the adsorption of OER intermediates [16]. In Fig. S16 in the ESM, the current density of a/c-CoFe-LDH shows an enhancement compared to that of CoFe-LDH, which indicates that the construction of amorphous/crystalline interface can enhance the absorption strength toward *OH. What is more, OOH*-related signal at 1220 cm^{-1} appeared in a/c-CoFe-LDH after OER in FTIR spectra, suggesting the existence of AEM pathway in a/c-CoFe-LDH as well (Fig. 4(i)) [60]. Therefore, the coupling effect of AEM and LOM can simultaneously accelerate the OER kinetics of a/c-CoFe-LDH.

The HER properties of a/c-CoFe-LDH/Pt, a/c-CoFe-LDH, and CoFe-LDH were investigated in 1.0 M KOH electrolyte. Among them, the a/c-CoFe-LDH/Pt exhibits the best HER performance with the overpotential of 84 mV at 10 $mA·cm^{-2}$. Besides, the overpotential of a/c-CoFe-LDH and CoFe-LDH is 283 and 290 mV, respectively (Fig. 5(a)). These results confirm the advantages of Pt nanoclusters in HER process. Compared to most reported LDH based catalysts, a/c-CoFe-LDH/Pt shows excellent HER activity (Fig. S18 in the ESM). In Fig. 5(b), a/c-CoFe-LDH/Pt (3.34 Ω) exhibits a lower R_{ct} compared to a/c-CoFe-LDH (3.68 Ω), implying accelerated HER kinetics. Besides, a/c-CoFe-LDH/Pt displays a Tafel slope of 126 $mV·dec^{-1}$, smaller than those of a/c-CoFe-LDH (132 $mV·dec^{-1}$) and CoFe-LDH (158 $mV·dec^{-1}$), demonstrating its promoted reaction kinetics (Fig. 5(c)). The mass activity of a/c-CoFe-LDH/Pt, a/c-CoFe-LDH, and CoFe-LDH is

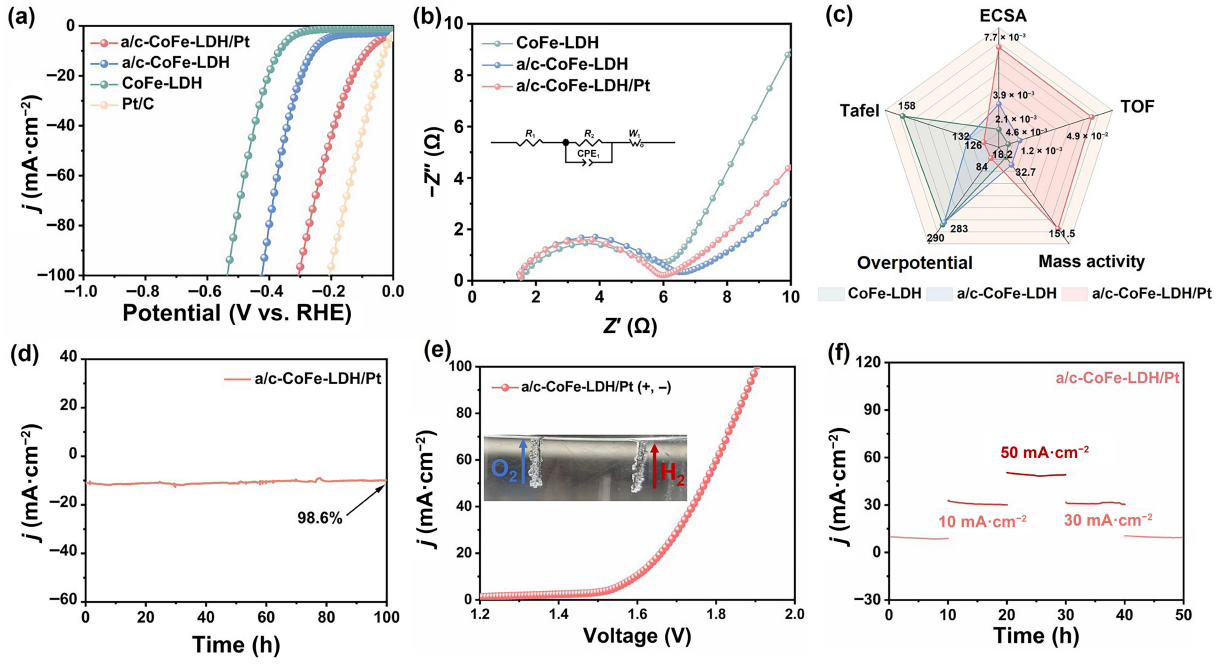

Figure 5 (a) LSV curves of a/c-CoFe-LDH/Pt, a/c-CoFe-LDH, CoFe-LDH, and RuO_2. (b) Nyquist plots with the fitting curves in HER. (c) Tafel, ECSA, TOF, overpotential, and mass activity of a/c-CoFe-LDH/Pt, a/c-CoFe-LDH, and CoFe-LDH. (d) Chronoamperometry test of a/c-CoFe-LDH/Pt in HER for 100 h. (e) Overall water splitting performance of a/c-CoFe-LDH/Pt (+, −). (f) Chronoamperometry curves of a/c-CoFe-LDH/Pt at a constant current density of 10, 30, and 50 $mA·cm^{-2}$.

151.5, 32.7, and 18.5 $mA·mg^{-1}$, respectively. In addition, the TOF of a/c-CoFe-LDH/Pt surpasses a/c-CoFe-LDH and CoFe-LDH as well. Besides, the ECSA-normalized LSV curves (Fig. S12(b) in the ESM) further validate that a/c-CoFe-LDH/Pt exhibits the highest HER activity. The results indicate that the catalyst with Pt nanocluster represents the highest intrinsic activity. Moreover, the long-term durability test demonstrates the superior stability of a/c-CoFe-LDH/Pt (Fig. 5(d) and Fig. S17(b) in the ESM). The introduction of Pt can resist structural collapse or phase separation which may occur during the reaction, thus enhancing the stability performance. The adsorbed hydrogen (H_{ad}) peak of a/c-CoFe-LDH is more positive than that of CoFe-LDH, demonstrating the stronger binding energies of H_{ad} (Fig. S13(a) in the ESM) [61]. The increased H_{ad} is attributed to metallization of low-valence state caused by the low coordination of amorphous CoFe-LDH and introduction of Pt, resulting in enhanced metal–H bond energy [36, 62]. In addition, this electrolyzer (a/c-CoFe-LDH/Pt) requires a small cell voltage of 1.58 V to achieve the current density of 10 $mA·cm^{-2}$ for water splitting, which is comparable to those reported outstanding water splitting catalysts (Fig. 5(e) and Fig. S19 in the ESM). The volume ratio of O_2 to H_2 generated in the electrolytic cell based on a/c-CoFe-LDH/Pt electrocatalyst was approximately 2:1 (Fig. S20 and Movie S1 in the ESM). Regarding the stability of electrolytic cell based on a/c-CoFe-LDH/Pt, there is no evident potential fluctuation at 10, 30, and 50 $mA·cm^{-2}$ current density, further confirming its satisfactory stability (Fig. 5(f)). The results of ICP-MS of electrolytes after OER/HER also confirmed the superior stability of a/c-CoFe-LDH/Pt in OER/HER (Table S3 in the ESM). Furthermore, the produced H_2 and O_2 were analyzed and collected using gas chromatography. The a/c-CoFe-LDH/Pt system exhibits a near 2:1 molar ratio of H_2 to O_2 (Fig. S21 in the ESM). The above results indicate that water is completely resolved into oxygen and hydrogen, indicating an almost 100% Faradaic efficiency.

To get in-depth understanding of the catalytic reaction of a/c-CoFe-LDH, the TEM and SEM images of the catalysts after OER and HER were tested. The ultrathin nanosheet structure of a/c-CoFe-LDH is maintained after OER, which proves their superior stability (Fig. S22(a) in the ESM). The lattice fringes of 1.95, 2.16, and 2.37 Å are ascribed to the (018) plane of CoFe-LDH, (210) plane of FeOOH (210) and (101) plane of CoOOH, respectively (Fig. S23(a) in the ESM). The CoOOH and FeOOH phases formed during the OER serve as the true active sites, effectively reducing the energy barrier for water oxidation owing to the optimal e_g orbitals occupancy in intermediate spin (IS) Co^{3+} and IS Fe^{3+} [27, 63]. Furthermore, the overall structure of a/c-CoFe-LDH remains original morphology after HER (Figs. S22(b) and S23(b) in the ESM). The HRTEM image confirms that the lattice fringe belongs to the (015) and (104) planes of CoFe-LDH, demonstrating that its stability during HER.

To investigate the influence of amorphous/crystalline heterostructure on the catalytic mechanism, DFT calculations were performed. According to Bader charge analysis, with the generation of amorphous structure, the concentration of oxygen vacancies increases, and the metal atoms in a/c-CoFe-LDH gain electrons, in good agreement with the XPS results (Fig. S24 in the ESM). Figure S25 in the ESM presents the structural models of the O_v in both a/c-CoFe-LDH and CoFe-LDH, respectively. The DFT calculation results reveal that the formation energy of O_v in a/c-CoFe-LDH (3.64 eV) is lower than that in a/c-CoFe-LDH (3.81 eV), which suggests that the presence of the amorphous phase facilitates the formation of O_v, thereby triggering LOM pathway for improved catalytic efficiency. The Gibbs free energies of a/c-CoFe-LDH and CoFe-LDH on the surface were calculated based on the models in Figs. S26–S29 in the ESM. In Fig. 6(a), the energy barrier for hydrogen adsorption (ΔG_{H^*}) of a/c-CoFe-LDH and CoFe-LDH is −0.45 and −0.61 eV, respectively, demonstrating the weaker adsorption of the *H caused by the amorphous phase. The Gibbs

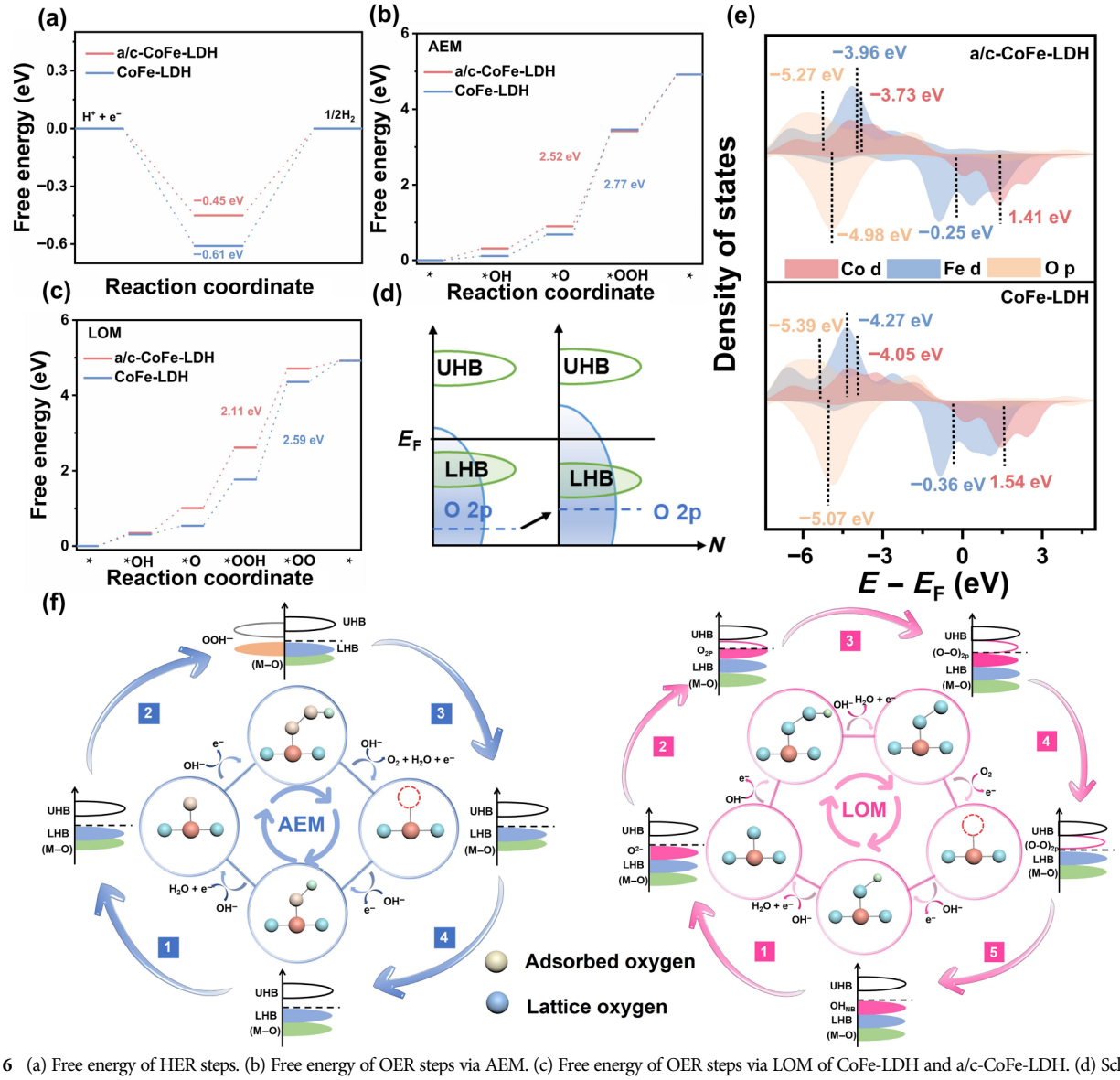

Figure 6 (a) Free energy of HER steps. (b) Free energy of OER steps via AEM. (c) Free energy of OER steps via LOM of CoFe-LDH and a/c-CoFe-LDH. (d) Schematic band diagrams (UHB: upper Hubbard band, LHB: lower Hubbard band, *N* (e): state density). (e) Metal 3d-band centers and O 2p-band centers of CoFe-LDH and a/c-CoFe-LDH. (f) AEM and LOM on CoFe-LDH and a/c-CoFe-LDH.

free energy, along with OER steps under AEM and LOM, is calculated to identify the energetics of OER steps of the catalysts. The related reaction intermediates models in AEM and LOM are presented in Figs. S26–S29 in the ESM. The OER steps on a/c-CoFe-LDH under AEM and LOM are described in Fig. 6(f). For AEM pathway, the rate determining step (RDS) is the formation of *OOH which shows corresponding energy barriers of 2.52 and 2.77 eV for a/c-CoFe-LDH and CoFe-LDH, respectively. The incorporation of amorphous structure induces the reduced energy barrier of AEM reaction. For comparison, the Gibbs free energy profiles of a/c-CoFe-LDH and CoFe-LDH following LOM are also provided (Fig. 6(c)). From the perspective of thermodynamics, a/c-CoFe-LDH with lower energy barrier prefers to follow LOM pathway, which is well consistent with the experimental results. In addition, a/c-CoFe-LDH and CoFe-LDH exhibit significant differences in the final step of the LOM pathway, which proves that spin effects indeed can enhance OER activity. The RDS of a/c-CoFe-LDH is the formation of O_2 with the Gibbs free energy (ΔG) of 2.11 eV, far smaller than that for AEM, indicating favorable lattice oxygen participation. Hence, the incorporation of amorphous CoFe-LDH is beneficial for simultaneously triggering the metal and lattice oxygen redox pair to promote OER kinetics. The density of states (DOS) results suggest that d orbitals of Co atoms and Fe atoms contribute to the DOS near Fermi levels (E_F), implying that the main active centers are Co and Fe sites in a/c-CoFe-LDH and CoFe-LDH (Fig. S30 in the ESM). In addition, the spin-up of 3d states of Fe atoms (0–0.2 eV) increases, which demonstrates that the Fe atoms becomes more active after the introduction of amorphous structure, thus reducing the free energies of oxygen-containing intermediates [64]. Also, the spin-up and spin-down states are revealed to better understand the changes in electronic structure (Fig. S31 in the ESM). After coupling with amorphous CoFe-LDH, more unbalanced states can be found on Co (~ 0.48e^- more) atoms and Fe (0.21e^- more) atoms in a/c-CoFe-LDH, indicating increased net spins. Therefore, the electrons can more freely occupy the e_g and a_{1g} orbitals in a/c-CoFe-LDH, leading to spin polarization,

which scales up the spin-dependent electron mobility [65, 66]. Compared to the CoFe-LDH with AFM, the a/c-CoFe-LDH with FM exhibits enhanced spin density localized on oxygen sites, which will facilitate spin-selective electron transfer and optimize the kinetics of the spin-charge transfer processes (Fig. S32 in the ESM). As shown in Fig. 6(e), the d-band center of Co and Fe in a/c-CoFe-LDH is closer to the Fermi level refer to that of CoFe-LDH, revealing the increasing antibonding energy states and enhanced binding strength. The O 2p band center of a/c-CoFe-LDH shifts towards E_F, which is favor of the release of the lattice oxygen, demonstrating that the incorporation of amorphous states is beneficial for triggering the LOM (Fig. 6(d)). The activated lattice oxygen can act as additional active sites and cooperate with metal active sites to promote electrocatalytic water splitting.

4 Conclusions

In summary, amorphous CoFe LDH/crystalline CoFe LDH nanosheet (a/c-CoFe-LDH) was prepared by acid-etching assisted coprecipitation method for overall electrochemical water splitting. Owing to the unsaturated coordination of amorphous CoFe-LDH, a/c-CoFe-LDH possesses oxygen non-bonding states and controllable spin states, thus triggering the LOM followed by promoted reaction kinetics. Meanwhile, the crystalline structure endows excellent intrinsic conductivity and persistent durability. The results reveal that the regulated spin state and optimized adsorption strength stemmed from the incorporation of amorphous structure favors for the improved catalytic activity. This work constructs a relationship between amorphous structure and spin configuration. The results reveal that amorphous structure could trigger the LOM, which offers new concept for design of efficient electrocatalysts.

Electronic Supplementary Material: Supplementary material (detailed analyses of SEM/TEM/AFM images, XRD patterns, BET results, XPS spectra, Raman spectroscopy, electrochemical measurements, DFT models and results, tables for the surface molar ratios of Co/Fe, and amorphous phase content) is available in the online version of this article at https://doi.org/10.26599/NR.2025.94907668.

Data availability

All data needed to support the conclusions in the paper are presented in the manuscript and the Electronic Supplementary Material. Additional data related to this paper may be requested from the corresponding author upon request.

Acknowledgements

This work was financially supported by the Natural Science Foundation of Hubei Province (Nos. 2024AFB836 and 2023AFB626), the National Natural Science Foundation of China (Nos. 22105151 and 52305211), the Knowledge Innovation Project of Wuhan, China (No. 2022010801010306), the Open Project of Key Laboratory of Green Chemical Engineering Process of Ministry of Education (No. GCP2022003), the Youth Science and Technology Zhaoyang Program of Wuhan (No. whkx202203), and "The 14th Five Year Plan" Hubei Provincial advantaged characteristics disciplines (groups) project of Wuhan University of Science and technology (No. 2023A0305). We would like to thank Ms. Lixia Fan and Mr. Juliang Xu at the Analytical & Testing Center of Wuhan University of Science and Technology for the help on SEM and XRD analysis.

Declaration of competing interest

All the contributing authors report no conflict of interests in this work.

Author contribution statement

L. Z. supervised this project. Y. C. revised the manuscript and triggered helpful discussion. C. G. and W. X. L. conceived the original concept, analyzed the data and wrote the paper. X. D. help performed synthesis and characterizations. C. G., X. H., and D. H. W. contributed electrochemical measurements and discussed the results. H. C. contributed the DFT calculations and analysis. W. F. conduct Raman test. All authors engaged in the analysis of experimental results and manuscript edition. All the authors have approved the final manuscript.

Use of AI statement

None.

References

[1] Li, H. Q.; Chen, L.; Jin, P. F.; Li, Y. F.; Pang, J. X.; Hou, J.; Peng, S. L.; Wang, G.; Shi, Y. L. $NiCo_2S_4$ microspheres grown on N, S co-doped reduced graphene oxide as an efficient bifunctional electrocatalyst for overall water splitting in alkaline and neutral pH. *Nano Res.* **2022**, *15*, 950–958.

[2] Li, D. M.; Li, W. X.; Gong, C.; He, X.; Wang, D. H.; Chen, H.; Fang, W.; Zeng, X. H.; Du, X.; Zhao, L. $Co(OH)_2$ confined in MIL-100 nanosheets with enriched oxygen vacancies for efficient electrocatalytic water splitting. *Appl. Surf. Sci.* **2024**, *669*, 160591.

[3] Gong, C.; Li, W. X.; Lei, Y. N.; He, X.; Chen, H.; Du, X.; Fang, W.; Wang, D. H.; Zhao, L. Interfacial engineering of ZIF-67 derived CoSe/$Co(OH)_2$ catalysts for efficient overall water splitting. *Compos. Part B: Eng.* **2022**, *236*, 109823.

[4] Karmakar, A.; Karthick, K.; Sankar, S. S.; Kumaravel, S.; Madhu, R.; Kundu, S. A vast exploration of improvising synthetic strategies for enhancing the OER kinetics of LDH structures: A review. *J. Mater. Chem. A* **2021**, *9*, 1314–1352.

[5] Gong, C.; Zhao, L.; Li, D. M.; He, X.; Chen, H.; Du, X.; Wang, D. H.; Fang, W.; Zeng, X. H.; Li, W. X. *In-situ* interfacial engineering of $Co(OH)_2/Fe_7Se_8$ nanosheets to boost electrocatalytic water splitting. *Chem. Eng. J.* **2023**, *466*, 143124.

[6] Guo, T. T.; Chen, L. Y.; Li, Y. W.; Shen, K. Controllable synthesis of ultrathin defect-rich LDH nanoarrays coupled with MOF-derived Co–NC microarrays for efficient overall water splitting. *Small* **2022**, *18*, 2107739.

[7] Gracia, J. Itinerant spins and bond lengths in oxide electrocatalysts for oxygen evolution and reduction reactions. *J. Phys. Chem. C* **2019**, *123*, 9967–9972.

[8] Zhang, Z. R.; Ma, P. Y.; Luo, L.; Ding, X. L.; Zhou, S. M.; Zeng, J. Regulating spin states in oxygen electrocatalysis. *Angew. Chem., Int. Ed.* **2023**, *62*, e202216837.

[9] Guo, T. Q.; Li, L. D.; Wang, Z. C. Recent development and future perspectives of amorphous transition metal-based electrocatalysts for oxygen evolution reaction. *Adv. Energy Mater.* **2022**, *12*, 2200827.

[10] Anantharaj, S.; Noda, S. Amorphous catalysts and electrochemical water splitting: An untold story of harmony. *Small* **2020**, *16*, 1905779.

[11] Zhang, X.; Zhong, H. Y.; Zhang, Q.; Zhang, Q. H.; Wu, C.; Yu, J. C.;

Ma, Y. F.; An, H.; Wang, H.; Zou, Y. M. et al. High-spin Co^{3+} in cobalt oxyhydroxide for efficient water oxidation. *Nat. Commun.* **2024**, *15*, 1383.

[12] Jin, Y. Z.; Li, Z.; Wang, J. Q.; Li, R.; Li, Z. Q.; Liu, H.; Mao, J.; Dong, C. K.; Yang, J.; Qiao, S. Z. et al. Tuning spin state of rock-salt-based oxides by manipulation of crystallinity for efficient oxygen electrocatalysis. *Adv. Energy Mater.* **2018**, *8*, 1703469.

[13] Li, L. F.; Zhang, X.; Humayun, M.; Xu, X. F.; Shang, Z. X.; Li, Z. S.; Yuen, M. F.; Hong, C. X.; Chen, Z. H.; Zeng, J. R. et al. Manipulation of electron spins with oxygen vacancy on amorphous/crystalline composite-type catalyst. *ACS Nano* **2024**, *18*, 1214–1225.

[14] Wang, X. P.; Zhong, H. Y.; Xi, S. B.; Lee, W. S. V.; Xue, J. M. Understanding of oxygen redox in the oxygen evolution reaction. *Adv. Mater.* **2022**, *34*, 2107956.

[15] Wang, F. Q.; Zou, P. C.; Zhang, Y. Y.; Pan, W. L.; Li, Y.; Liang, L. M.; Chen, C.; Liu, H.; Zheng, S. J. Activating lattice oxygen in high-entropy LDH for robust and durable water oxidation. *Nat. Commun.* **2023**, *14*, 6019.

[16] Xin, S. S.; Tang, Y.; Jia, B. H.; Zhang, Z. F.; Li, C. P.; Bao, R.; Li, C. J.; Yi, J. H.; Wang, J. S.; Ma, T. Y. Coupling adsorbed evolution and lattice oxygen mechanism in Fe–$Co(OH)_2$/Fe_2O_3 heterostructure for enhanced electrochemical water oxidation. *Adv. Funct. Mater.* **2023**, *33*, 2305243.

[17] Zhao, W. P.; Zhang, Q. C.; Zhu, Y. Z.; Zhao, P. W.; Chen, B.; Peng, W. C.; Li, Y.; Zhang, F. B.; Fan, X. B. Boosting reaction kinetics and mass transfer of bifunctional Co-based oxygen electrocatalyst prepared from CoAl-LDH. *Adv. Energy Mater.* **2023**, *13*, 2301580.

[18] Singh, M.; Cha, D. C.; Singh, T. I.; Maibam, A.; Paudel, D. R.; Nam, D. H.; Kim, T. H.; Yoo, S.; Lee, S. A critical review on amorphous–crystalline heterostructured electrocatalysts for efficient water splitting. *Mater. Chem. Front.* **2023**, *7*, 6254–6280.

[19] Zhou, D. J.; Wang, S. Y.; Jia, Y.; Xiong, X. Y.; Yang, H. B.; Liu, S.; Tang, J. L.; Zhang, J. M.; Liu, D.; Zheng, L. R. et al. NiFe hydroxide lattice tensile strain: Enhancement of adsorption of oxygenated intermediates for efficient water oxidation catalysis. *Angew. Chem., Int. Ed.* **2019**, *58*, 736–740.

[20] Xue, H. Y.; Yang, T. Q.; Zhang, Z. M.; Zhang, Y. X.; Geng, Z. H.; He, Y. Stimulate the hidden catalysis potential and exposure of nickel site in NiSe@CNTs result in ultra-high HER/OER activity and stability. *Appl. Catal. B: Environ.* **2023**, *330*, 122641.

[21] Jiang, Z. Z.; Zhou, W. D.; Hu, C.; Luo, X. F.; Zeng, W.; Gong, X. G.; Yang, Y.; Yu, T.; Lei, W.; Yuan, C. L. Interlayer-confined NiFe dual atoms within MoS_2 electrocatalyst for ultra-efficient acidic overall water splitting. *Adv. Mater.* **2023**, *35*, 2300505.

[22] Huo, J. M.; Wang, Y.; Meng, J.; Zhao, X. Y.; Zhai, Q. G.; Jiang, Y. C.; Hu, M. C.; Li, S. N.; Chen, Y. $\pi\cdots\pi$ interaction directed 2D FeNi-LDH nanosheets from 2D Hofmann-MOFs for the oxygen evolution reaction. *J. Mater. Chem. A* **2022**, *10*, 1815–1820.

[23] Liu, Y.; Liu, X. H.; Jadhav, A. R.; Yang, T.; Hwang, Y.; Wang, H. D.; Wang, L. L.; Luo, Y. G.; Kumar, A.; Lee, J. et al. Unraveling the function of metal–amorphous support interactions in single-atom electrocatalytic hydrogen evolution. *Angew. Chem.* **2022**, *134*, e202114160.

[24] Lin, J. F.; Speziale, S.; Mao, Z.; Marquardt, H. Effects of the electronic spin transitions of iron in lower mantle minerals: Implications for deep mantle geophysics and geochemistry. *Rev. Geophys.* **2013**, *51*, 244–275.

[25] Sun, S. N.; Sun, Y. M.; Zhou, Y.; Shen, J. J.; Mandler, D.; Neumann, R.; Xu, Z. J. Switch of the rate-determining step of water oxidation by spin-selected electron transfer in spinel oxides. *Chem. Mater.* **2019**, *31*, 8106–8111.

[26] Sun, Y. M.; Ren, X.; Sun, S. N.; Liu, Z.; Xi, S. B.; Xu, Z. J. Engineering high-spin state cobalt cations in spinel zinc cobalt oxide for spin channel propagation and active site enhancement in water oxidation. *Angew. Chem.* **2021**, *133*, 14657–14665.

[27] Zhou, F.; Gong, Z. Q.; Wang, R. H.; Guo, M. R.; Zeng, R.; Li, Y.; Xiao, Z.; Qie, L.; Liu, J. W. Band structure and spin-state-induced electronic configuration regulation for efficient sulfur redox reaction. *Adv. Funct. Mater.* **2025**, *35*, 2417730.

[28] Zhang, Y. W.; Wu, Q.; Seow, J. Z. Y.; Jia, Y. J.; Ren, X.; Xu, Z. C. J. Spin states of metal centers in electrocatalysis. *Chem. Soc. Rev.* **2024**, *53*, 8123–8136.

[29] Wang, Y. H.; Li, S. Q.; Hou, X.; Cui, T. T.; Zhuang, Z. C.; Zhao, Y. H.; Wang, H. Z.; Wei, W.; Xu, M.; Fu, Q. et al. Low-spin Fe^{3+} evoked by multiple defects with optimal intermediate adsorption attaining unparalleled performance in water oxidation. *Adv. Mater.* **2024**, *36*, 2412598.

[30] Mei, Z. Y.; Zhao, G. F.; Xia, C. F.; Cai, S.; Jing, Q.; Sheng, X. L.; Wang, H.; Zou, X. X.; Wang, L. L.; Guo, H. et al. Regulated high-spin state and constrained charge behavior of active cobalt sites in covalent organic frameworks for promoting electrocatalytic oxygen reduction. *Angew. Chem.* **2023**, *135*, e202303871.

[31] Zhang, H. Y.; Wu, L. L.; Feng, R. H.; Wang, S. H.; Hsu, C. S.; Ni, Y. M.; Ahmad, A.; Zhang, C. R.; Wu, H. F.; Chen, H. M. et al. Oxygen vacancies unfold the catalytic potential of NiFe-layered double hydroxides by promoting their electronic transport for oxygen evolution reaction. *ACS Catal.* **2023**, *13*, 6000–6012.

[32] Zhang, J. Y.; Yan, Y.; Mei, B. B.; Qi, R. J.; He, T.; Wang, Z. T.; Fang, W. S.; Zaman, S.; Su, Y. Q.; Ding, S. J. et al. Local spin-state tuning of cobalt–iron selenide nanoframes for the boosted oxygen evolution. *Energy Environ. Sci.* **2021**, *14*, 365–373.

[33] Sun, Y. M.; Sun, S. N.; Yang, H. T.; Xi, S. B.; Gracia, J.; Xu, Z. J. Spin-related electron transfer and orbital interactions in oxygen electrocatalysis. *Adv. Mater.* **2020**, *32*, 2003297.

[34] Reith, L.; Hausmann, J. N.; Mebs, S.; Mondal, I.; Dau, H.; Driess, M.; Menezes, P. W. *In-situ* detection of iron in oxidation states ≥ IV in cobalt–iron oxyhydroxide reconstructed during oxygen evolution reaction. *Adv. Energy Mater.* **2023**, *13*, 2203886.

[35] Wu, J. S.; Yang, T.; Fu, R.; Zhou, M.; Xia, L. X.; Wang, Z. Y.; Zhao, Y. Constructing electrocatalysts with composition gradient distribution by solubility product theory: Amorphous/crystalline CoNiFe-LDH hollow nanocages. *Adv. Funct. Mater.* **2023**, *33*, 2300808.

[36] Huo, J. M.; Ma, Z. L.; Wang, Y.; Cao, Y. J.; Jiang, Y. C.; Li, S. N.; Chen, Y.; Hu, M. C.; Zhai, Q. G. Monodispersed Pt sites supported on NiFe-LDH from synchronous anchoring and reduction for high efficiency overall water splitting. *Small* **2023**, *19*, 2207044.

[37] Yao, Y. C.; Yang, C. X.; Sun, S. J.; Zhang, H.; Geng, M. Q.; He, X.; Dong, K.; Luo, Y. L.; Zheng, D. D.; Zhuang, W. H. et al. Boosting alkaline seawater oxidation of CoFe-layered double hydroxide nanosheet array by Cr doping. *Small* **2024**, *20*, 2307294.

[38] Sun, H. C.; Li, J. G.; Lv, L.; Li, Z. S.; Ao, X.; Xu, C. H.; Xue, X. Y.; Hong, G.; Wang, C. D. Engineering hierarchical CoSe/NiFe layered-double-hydroxide nanoarrays as high efficient bifunctional electrocatalyst for overall water splitting. *J. Power Sources* **2019**, *425*, 138–146.

[39] Qiang, R.; Wang, H.; Xu, K.; Yuan, Q. Y.; Yu, Y. X.; Li, L.; Wang, J. O.; Zheng, L. R.; Sherrell, P. C.; Chen, J. et al. Available active sites on ε-Fe_3N nanoparticles synthesized by a facile route for hydrogen evolution reaction. *Adv. Mater. Interfaces* **2021**, *8*, 2100070.

[40] Zhang, Q.; Xiao, W.; Guo, W. H.; Yang, Y. X.; Lei, J. L.; Luo, H. Q.; Li, N. B. Macroporous array induced multiscale modulation at the surface/interface of $Co(OH)_2$/NiMo self-supporting electrode for effective overall water splitting. *Adv. Funct. Mater.* **2021**, *31*, 2102117.

[41] Wang, Y. H.; Li, L.; Shi, J. H.; Xie, M. Y.; Nie, J. H.; Huang, G. F.; Li, B.; Hu, W. Y.; Pan, A. L.; Huang, W. Q. Oxygen defect engineering promotes synergy between adsorbate evolution and single lattice oxygen mechanisms of OER in transition metal-based (oxy) hydroxide. *Adv. Sci.* **2023**, *10*, 2303321.

[42] Zhou, G.; Wang, P. F.; Li, H.; Hu, B.; Sun, Y.; Huang, R.; Liu, L. Z. Spin-state reconfiguration induced by alternating magnetic field for efficient oxygen evolution reaction. *Nat. Commun.* **2021**, *12*, 4827.
[43] Goodenough, J. B. Goodenough–Kanamori rule. *Scholarpedia* **2008**, *3*, 7382.
[44] Wang, Y.; Yang, C. X.; Li, Z. M.; Liang, Z. Z.; Cao, G. Z. The $-NH_x$ group induced formation of 3D α-$Co(OH)_2$ curly nanosheet aggregates as efficient oxygen evolution electrocatalysts. *Small* **2020**, *16*, 2001973.
[45] Zhong, H. H.; Liu, T. Y.; Zhang, S. W.; Li, D. Q.; Tang, P. G.; Alonso-Vante, N.; Feng, Y. J. Template-free synthesis of three-dimensional NiFe-LDH hollow microsphere with enhanced OER performance in alkaline media. *J. Energy Chem.* **2019**, *33*, 130–137.
[46] Liu, S. L.; Wan, R. D.; Lin, Z. S.; Liu, Z.; Liu, Y. G.; Tian, Y.; Qin, D. D.; Tang, Z. H. Probing the Co role in promoting the OER and Zn–air battery performance of NiFe-LDH: A combined experimental and theoretical study. *J. Mater. Chem. A* **2022**, *10*, 5244–5254.
[47] Sun, F. Z.; Li, C. Q.; Li, B.; Lin, Y. Q. Amorphous MoS_x developed on $Co(OH)_2$ nanosheets generating efficient oxygen evolution catalysts. *J. Mater. Chem. A* **2017**, *5*, 23103–23114.
[48] Dai, L.; Chen, Z. N.; Li, L. X.; Yin, P. Q.; Liu, Z. Q.; Zhang, H. Ultrathin Ni(0)-embedded $Ni(OH)_2$ heterostructured nanosheets with enhanced electrochemical overall water splitting. *Adv. Mater.* **2020**, *32*, 1906915.
[49] Sakita, A. M. P.; Noce, R. D.; Vallés, E.; Benedetti, A. V. Pulse electrodeposition of CoFe thin films covered with layered double hydroxides as a fast route to prepare enhanced catalysts for oxygen evolution reaction. *Appl. Surf. Sci.* **2018**, *434*, 1153–1160.
[50] Chen, W. B.; Wang, C. S.; Su, S. B.; Wang, H.; Cai, D. D. Synthesis of ZIF-9 (III)/Co LDH layered composite from ZIF-9 (I) based on controllable phase transition for enhanced electrocatalytic oxygen evolution reaction. *Chem. Eng. J.* **2021**, *414*, 128784.
[51] Huang, Y. W.; Wei, G. J.; He, J.; An, C. H.; Hu, M.; Shu, M.; Zhu, J. F.; Yao, S.; Xi, W.; Si, R. et al. Interfacial electronic interaction of atomically dispersed $IrCl_x$ on ultrathin $Co(OH)_2$/CNTs for efficient electrocatalytic water oxidation. *Appl. Catal. B: Environ.* **2020**, *279*, 119398.
[52] Chen, M. X.; Li, H. J.; Wu, C. L.; Liang, Y. B.; Qi, J.; Li, J.; Shangguan, E. B.; Zhang, W.; Cao, R. Interfacial engineering of heterostructured $Co(OH)_2/NiP_x$ nanosheets for enhanced oxygen evolution reaction. *Adv. Funct. Mater.* **2022**, *32*, 2206407.
[53] Kuznetsov, D. A.; Han, B. H.; Yu, Y.; Rao, R. R.; Hwang, J.; Román-Leshkov, Y.; Shao-Horn, Y. Tuning redox transitions via inductive effect in metal oxides and complexes, and implications in oxygen electrocatalysis. *Joule* **2018**, *2*, 225–244.
[54] Ding, J. T.; Guo, D. Y.; Wang, N. S.; Wang, H. F.; Yang, X. F.; Shen, K.; Chen, L. Y.; Li, Y. W. Defect engineered metal–organic framework with accelerated structural transformation for efficient oxygen evolution reaction. *Angew. Chem., Int. Ed.* **2023**, *62*, e202311909.
[55] Zhai, P. L.; Wang, C.; Zhao, Y. Y.; Zhang, Y. X.; Gao, J. F.; Sun, L. C.; Hou, J. G. Regulating electronic states of nitride/hydroxide to accelerate kinetics for oxygen evolution at large current density. *Nat. Commun.* **2023**, *14*, 1873.
[56] Li, X.; Deng, C.; Kong, Y.; Huo, Q. H.; Mi, L. R.; Sun, J. J.; Cao, J. Y.; Shao, J. X.; Chen, X. B.; Zhou, W. L. et al. Unlocking the transition of electrochemical water oxidation mechanism induced by heteroatom doping. *Angew. Chem., Int. Ed.* **2023**, *62*, e202309732.
[57] Wang, T. J.; Liu, X. Y.; Li, Y.; Li, F. M.; Deng, Z. W.; Chen, Y. Ultrasonication-assisted and gram-scale synthesis of Co-LDH nanosheet aggregates for oxygen evolution reaction. *Nano Res.* **2020**, *13*, 79–85.
[58] Han, X. T.; Yu, C.; Niu, Y. Y.; Wang, Z.; Kang, Y. B.; Ren, Y. W.; Wang, H.; Park, H. S.; Qiu, J. S. Full bulk-structure reconstruction into amorphorized cobalt–iron oxyhydroxide nanosheet electrocatalysts for greatly improved electrocatalytic activity. *Small Methods* **2020**, *4*, 2000546.
[59] Lin, C.; Li, J. L.; Li, X. P.; Yang, S.; Luo, W.; Zhang, Y. J.; Kim, S. H.; Kim, D. H.; Shinde, S. S.; Li, Y. F. et al. *In-situ* reconstructed Ru atom array on α-MnO_2 with enhanced performance for acidic water oxidation. *Nat. Catal.* **2021**, *4*, 1012–1023.
[60] Wang, A. S.; Wang, W. Y.; Xu, J. C.; Zhu, A.; Zhao, C. N.; Yu, M.; Shi, G. L.; Yan, J. G.; Sun, S. H.; Wang, W. C. Enhancing oxygen evolution reaction by simultaneously triggering metal and lattice oxygen redox pair in iridium loading on Ni-doped Co_3O_4. *Adv. Energy Mater.* **2023**, *13*, 2302537.
[61] Wang, L. Q.; Xu, Z. P.; Kuo, C. H.; Peng, J.; Hu, F.; Li, L. L.; Chen, H. Y.; Wang, J. Z.; Peng, S. J. Stabilizing low-valence single atoms by constructing metalloid tungsten carbide supports for efficient hydrogen oxidation and evolution. *Angew. Chem., Int. Ed.* **2023**, *62*, e202311937.
[62] Yang, H. Y.; Chen, Z. L.; Guo, P. F.; Fei, B.; Wu, R. B. B-doping-induced amorphization of LDH for large-current-density hydrogen evolution reaction. *Appl. Catal. B: Environ.* **2020**, *261*, 118240.
[63] Chen, H.; Liang, X.; Liu, Y. P.; Ai, X.; Asefa, T.; Zou, X. X. Active site engineering in porous electrocatalysts. *Adv. Mater.* **2020**, *32*, 2002435.
[64] Jia, Z. C.; Yuan, Y.; Zhang, Y. X.; Lyu, X.; Liu, C. H.; Yang, X. L.; Bai, Z. Y.; Wang, H. J.; Yang, L. Optimizing 3d spin polarization of CoOOH by *in-situ* Mo doping for efficient oxygen evolution reaction. *Carbon Energy* **2024**, *6*, e418.
[65] Zhou, G.; Wang, P. F.; Hu, B.; Shen, X. Y.; Liu, C. C.; Tao, W. X.; Huang, P. L.; Liu, L. Z. Spin-related symmetry breaking induced by half-disordered hybridization in $Bi_xEr_{2-x}Ru_2O_7$ pyrochlores for acidic oxygen evolution. *Nat. Commun.* **2022**, *13*, 4106.
[66] Wu, T. Z.; Sun, Y. M.; Ren, X.; Wang, J. R.; Song, J. J.; Pan, Y. D.; Mu, Y. B.; Zhang, J. S.; Cheng, Q. Z.; Xian, G. Y. et al. Reconstruction of thiospinel to active sites and spin channels for water oxidation. *Adv. Mater.* **2023**, *35*, 2207041.